Ageing-resistant zirconia/graphene-based nanostructures composites for use as biomaterials

Ana Morales-Rodríguez[1,*], Carmen González-Orellana[1], Antonio A. Pérez-García[1], Cristina López-Pernía[1], Carmen Muñoz-Ferreiro[1], Rosalía Poyato[2], Ángela Gallardo-López[1].

[1]Depto. de Física de la Materia Condensada, ICMS, CSIC-Universidad de Sevilla, Apdo. 1065, 41080 Sevilla, Spain.

[2]Instituto de Ciencia de Materiales de Sevilla, ICMS, CSIC-Universidad de Sevilla, Avda. Américo Vespucio 49, 41092 Sevilla, Spain.

*Corresponding author. E-mail address: amr@us.es

Abstract

This work explores the incorporation of graphene-based two-dimensional nanostructures as moisture barriers to delay hydrothermal ageing of yttria-stabilized zirconia and strengthen its use in biomedical applications. Two sets of highly dense zirconia composites incorporating multilayered graphene with very different lateral dimensions, few layer graphene and exfoliated graphene nanoplatelets, were prepared. The effect of the addition of graphene nanostructures on zirconia ageing was investigated by conducting accelerated hydrothermal degradation experiments in an autoclave. An improved resistance to low-temperature degradation and a high tolerance to damage were achieved in the composites compared to those of monolithic zirconia. The incorporation of 1 vol% multilayered graphene was very effective in restricting the hydrothermal degradation. In particular, the composite incorporating exfoliated graphene nanosheets exhibited outstanding resistance to ageing because of their fine dispersion throughout the matrix, which effectively seemed to restrict grain growth and slow the propagation of the transformation front to the ceramic bulk.

Keywords: graphene-based nanostructures; yttria tetragonal zirconia; spark plasma sintering; low temperature degradation.

1. INTRODUCTION

The progress of ceramic materials for medical and engineering uses is improving due to their high strength and hardness, chemical inertness, and thermal insulation properties, although their inherent brittleness is still a limitation for widespread use. Yttria-stabilized tetragonal zirconia polycrystal (Y-TZP) is a high-tech ceramic used in wear resistance components, ionic conductive devices, and dental implantology, but its application as a biomaterial in knee and hip orthopaedic prostheses is very limited due to its lack of long-term stability in aqueous environments as biological fluids of human bodies [1–3]. Low-temperature degradation (LTD), also known as hydrothermal ageing, involves the spontaneous transformation of metastable tetragonal grains into monoclinic phase below 400 ° C in the presence of water. Transformation progresses from the surface in contact with water to the bulk and promotes surface roughening, grain pull-out and microcracks, deteriorating the high-performance mechanical properties of tetragonal zirconia ceramics [3,4]. It is widely accepted that oxygen vacancy annihilation plays a dominant role in low-temperature degradation [3,5]. The increase in resistance to ageing by diminishing the transformability of the tetragonal zirconia phase, for example by reducing the grain size of the zirconia, negatively affects the inherent fracture toughness of Y-TZP ceramics, as a more stable tetragonal phase also implies the loss of the transformation toughening mechanism [4,6]. The development of new zirconia-based materials that combine transformation toughening with resistance to hydrothermal ageing is being investigated by approaches that focus mainly on minimizing the number of oxygen vacancies or minimizing the contact between zirconia grains [3].

In the last two decades, the enhancement of ceramic toughness through the incorporation of flexible carbon nanostructures joined to ceramic grains has received strong attention [6–10]. An intense research activity is focused on the development of graphene-reinforced ceramics with the aim of transferring the outstanding mechanical properties of graphene to the ceramic system [9–12]. A wide variety of graphene-based 2D nanomaterials (GBN) is used as fillers for ceramic composites. By the number of graphene sheets, two groups are usually distinguished: multilayered graphene (MLG, with less than 10 layers of graphene) -where the subsets known as reduced graphene oxide (rGO) and few layer graphene (FLG, with 2 to about 5 layers) are included- and graphene nanoplatelets (GNP, with more than 10 layers and with a thickness lower than 100 nm).

Zirconia composites with GBN addition have shown toughness enhancement by graphene pullout, bridging, crack deflection and crack branching mechanisms [12–20]. In 3Y-TZP composites with GNP addition, fracture toughness –measured by single edge-notched beam method– increased by ~ 16% with the incorporation of GNP up to 1 wt% and decreased with an additional increase in the GNP content [14]. Su *et al* [16] reported a maximum increase by ~ 36% in the indentation fracture toughness of a 5 mol% Y_2O_3-TZP matrix composite with 0.5 wt% FLG content compared to monolithic ceramic. The further increase in FLG content also resulted in an impaired toughening effect, probably due to the presence of agglomerates. Energy dissipation by pull-out of graphene nanosheets decreases with the increasing number of graphene layers due to the weak bonding between them [16]. Compared to the moderate or even zero increase in fracture toughness reported for small GNP addition [15,16,21], the fracture toughness of zirconia

composites increased with rGO incorporation [13,18]. Shin and Hong [13] reported that the addition of rGO increased fracture toughness from 4.4 to 5.9 $MPa \cdot m^{1/2}$ at 4.1 vol% rGO content as a result of the grain wrapping with 2D graphene sheets. The most significant improvement is obtained in composites with *in-situ* reduced GO achieved during the spark plasma sintering process rather than in cases with prereduced graphene oxide toughened zirconia, associated with the formation of a C-O-Zr bond at the zirconia/rGO interface in addition to the conventional toughening mechanisms [18]. Fracture toughness of *in situ* reduced graphene oxide toughened zirconia composites increases markedly by up to ~ 75% with 0.09 wt% GO addition [18].

The development of bidimensional GBN-reinforced zirconia composites opens the way to the design of zirconia materials that combine improved fracture toughness [11-20] with better resistance to hydrothermal ageing. Since GBN have the advantage of impermeability to moisture and other gases [22–24] along with their high specific surface area, they provide a better coverage of grains for the same amount of material than using 1D or 3D fillers. Hydrothermal degradation has been shown to be strongly restricted in spark plasma sintered 3Y-TZP with 1D carbon nanotubes (CNT) [6,25,26]. Garmendia et al. [6] showed that the addition of a small volume fraction of multiwalled carbon nanotubes in 3Y-TZP leads to a promising balance between ageing and resistance to crack propagation. Furthermore, low temperature degradation decreases by adding CNT to 3Y-TZP compared to the ageing rate of monolithic ceramics [26,27], in a stronger way by incorporating multi-walled CNT [26] than single-walled CNT [27]. Incorporation of impermeable 2D GBN has been successfully used to prevent the penetration of moisture into polymers and inorganic compounds [28–36]. Concerning bulk polymeric composites, a significant enhancement in reducing the permeability of water vapor within the polymeric composites is achieved by increasing the graphene nanostructures content, their aspect ratio and exfoliation degree, as well as their preferential orientation through the in-plane direction [28]. Graphene-based coatings also serve as barriers to electrochemical corrosion in aqueous media, enhancing corrosion resistance in pure metals [30]. Wang et al. [33] demonstrated the effectiveness of graphene films as moisture barrier layers in inhibiting water-induced corrosion of silicate glasses. The introduction of rGO flakes mitigates the water-induced oxidation in PbS solar cells, yielding increased device stability in humid conditions [34]. Furthermore, the ambient stability of perovskite solar cells under an average relative humidity ~ 40% can be significantly improved by the introduction of rGO into the hole transport material layer [35]. Although the use of bidimensional carbon nanostructures is very effective in preventing water vapor permeability in polymer, metal, and ceramic systems, studies devoted to clarifying the influence of the incorporation of GBN on the hydrothermal degradation of zirconia are very scarce to date. To the best of our knowledge, only S. Li *et al.* [14] reported that graphene-platelet-reinforced zirconia composites exhibit less variation in monoclinic content than monolithic zirconia after ageing at 134 ° C for 24 h. The study was based on a qualitative comparison of the intensity of tetragonal and monoclinic diffraction peaks in the XRD patterns of aged samples.

This work proposes the incorporation of 2D graphene-based nanostructures acting as moisture barriers to reduce the susceptibility to ageing of 3Y-TZP ceramics. Two types of MLG, mainly differing in lateral size, -commercial few layer graphene (FLG, lateral dimension ≤ 10 μm) and exfoliated graphene nanoplatelets (e-GNP, lateral dimension ≤ 0.6 μm)- were incorporated with different MLG vol% (1, 2.5 and 5) in zirconia to compare their effectiveness in reducing the ageing rate. Ageing experiments accelerated in the autoclave were conducted at increasing exposure times. The change in the monoclinic phase content after each ageing step was evaluated by XRD to establish the hydrothermal ageing kinetics of these materials. Finally, the ageing response was also studied after 24 hours in two other composites prepared with GNP or *in situ* reduced GO to evaluate the influence of the graphene type. The main objective of this study is to elucidate the effect of the different MLG addition on the spontaneous transformation of the tetragonal zirconia ceramic under hydrothermal conditions and to evaluate the structural performance of these zirconia/MLG composites as biomaterials.

2. MATERIALS AND METHOD

2.1 Material processing

Partially-stabilized zirconia powder with uniform dispersion of 3 mol% yttria was used as ceramic component (ref. TZ-3YB-E, Tosoh Corporation, Tokyo, Japan). This biomedical-grade 3Y-TZP powder of 40 nm particle size containing controlled alumina doping (~0.1-0.4 wt%) is well-known for its improved resistance to ageing. The as-received zirconia powder was thermally treated at 850 ° C for 30 min in air as described elsewhere [37]. Two different graphene-based nanomaterials supplied by Angstrom Materials (Dayton, Ohio, USA) were added to the zirconia powder to prepare the composites: (i) few layer graphene (FLG, lateral dimension ≤ 10 μm and ≤ 3 graphene layers, ref. N002-PDR-HD) and (ii) graphene nanoplatelets (GNP, lateral dimension < 5 μm and 10-20 nm thickness, ref. N006-P).

Two different homogeneization routines were followed to prepare the two sets of composite powders with MLG contents of 1, 2.5 and 5 vol%. For the composites hereinafter named as FLG composites, the as-received FLG were subjected to bath ultrasonication (Clifton^{TM}, Fischer Scientific S.L., Madrid, Spain) in isopropanol for 30 min and additionally mixed and ultrasonicated with the ceramic powder for 5 min. The resulting powders obtained after drying on a hot plate with magnetic agitation were finally homogenized in an agate mortar. For the composites hereinafter referred to as e-GNP composites, the as-received GNP and zirconia powders were planetary ball milled (Pulverisette 7, Fritsch classic line) under dry conditions for 4 hours at 350 r.p.m. For each composition, 4 g of composite powders were introduced in a 45 ml zirconia jar with seven 15 mm diameter zirconia balls with a powder-to-ball weight ratio of 1:20. Planetary milling under dry conditions fractures the GNP and also promotes their exfoliation. This milling process changes the original structure of GNP to multilayered graphene [38,39]. The exfoliated GNP (e-GNP) show a drastically reduced lateral size (≤ 0.6 μm) and

thickness (less than 10 graphene layers) compared to the as-received GNP [38,39]. This processing route enables the preparation of composites with MLG addition that can be easily obtained from cost-effective graphene nanoplatelets.

Cylindrical samples of 15 mm diameter and ~3 mm thickness were sintered in a SPS apparatus (Model 515S, SPS Dr Sinter Inc., Kanagawa, Japan, Centro de Investigación, Tecnología e Innovación de la Universidad de Sevilla, CITIUS) operating under vacuum. For easy specimen removal, graphite paper was inserted between the powders (~3 g) and the cylindrical graphite die/punch setup. Uniaxial pressure of 75 MPa and holding time of 5 minutes at sintering temperature (1250 °C, 1300 ºC) were selected to achieve highly dense composites. Furthermore, monolithic zirconia samples were sintered at 1250 °C as reference material. Table 1 specifies the nominal graphene content, the MLG type present in sintered composites and the sintering temperature used for each studied material.

Table 1. List of sintered samples. The material reference first indicates its nominal filler content followed by the MLG type in the composite and the sintering temperature used.

Filler content (%vol)	MLG type	SPS temperature (ºC)	Material
-	-	1250	3Y-TZP1250
1	FLG	1250	1FLG1250
	e-GNP		1e-GNP1250
2.5	FLG	1300	2.5FLG1300
	e-GNP		2.5e-GNP1300
5	FLG	1250	5FLG1250
		1300	5FLG1300
	e-GNP	1300	5e-GNP1300

Two other composites were prepared with 2.5 vol% GNP or 2.5 vol% *in situ* reduced GO (rGO) for the sake of comparison. Details of the processing procedure and microstructural characterization can be found elsewhere [37,40]. The GNP composite was prepared by mixing the as-received GNP with the zirconia powder using probe ultrasonication following a wet ultrasonic processing routine similar to the one used to prepare the FLG/3Y-TZP composites as described in ref. [37]. The rGO composite was prepared by mixing graphene oxide (GO) with zirconia powder by a combination of probe ultrasonication and planetary ball milling in wet conditions, as described in ref. [40].

In summary, two sets with 1, 2.5 and 5 vol% multilayered graphene were prepared: as-received FLG (FLG) and exfoliated GNP (e-GNP). Two additional composites with 2.5 vol% as-received GNP (hereinafter referred to as 2.5GNP) or *in situ* reduced GO (referred to as 2.5rGO) were also prepared to establish a comparison between the different graphene nanostructures used as fillers.

2.2 Microstructural characterization

The bulk densities of the as-sintered materials were measured by the Archimedes' method using distilled water as immersion medium. The theoretical density of the composites was calculated using the mixture rule from density values of 6.05 $g \cdot cm^{-3}$ for 3Y-TZP and 2.2 $g \cdot cm^{-3}$ for GBN (data from the suppliers).

Possible structural modifications of the bidimensional graphene nanostructures after the composites processing and sintering were assessed by Raman spectroscopy using a LabRam HR800 spectrometer (Horiba Jobin Yvon, Kyoto, Japan) operating with a 20 mW He-Ne green laser (Instituto de Ciencias de Materiales de Sevilla, ICMS). Five to ten spectra were acquired on the as-received GNP and FLG, and on the fracture surfaces of the sintered composites. The first-order Raman spectra (from 1000 to 2000 cm^{-1}) were fitted to a sum of five functions (two Gaussian and three pseudo-Voigt functions), in order to obtain the intensities of the different Raman bands by means of their integrated areas, as previously described [15,38,40–42]. In the second order spectra (from 2250 to 3000 cm^{-1}), the best fit was achieved using three Lorentz functions and two pseudo-Voigt functions, as previously described [15,38,40–42]. Fits were carried out using the OriginLab software.

Zirconia crystalline structures and phase fractions were evaluated by XRD measurements on polished surfaces of the as-sintered samples. The XRD patterns were acquired in a diffractometer in Bragg–Brentano configuration (Bruker D8 Advance A25, Bruker Co, Germany) equipped with a Lynxeye PSD detector (Bruker, Germany) with 0.5º fix slit in the incident beam and axial Soller slits of 2.5º in the incident and diffracted beams for copper K_α radiation (CITIUS, Universidad de Sevilla, Spain). The diffracted intensity of a large number of reflection peaks was recorded over a wide range of 2θ diffraction angles (between 10 ° and 120°), with a step of 0.015 ° and a time per step of 0.5 s to ensure a large number of counts for each diffraction peak as required to carry out a robust quantitative analysis [43]. TOPAS 5.0 software from Bruker [44] was used to quantify zirconia crystallographic phases by Rietveld analysis [43]. Geometric factors were used for the measurement configuration. The background was fitted by a fourth–order Chebyshev polynomial, and zero error peak shift, absorption, lattice parameter of the cubic phase, and no-special sites in tetragonal and monoclinic structures were refined to provide the best fitting. Eighth-order spherical harmonic series were considered for the correction of preferred orientation effects in the cubic and tetragonal phase refinements.

High–resolution scanning electron microscopes (CITIUS, Universidad de Sevilla, Spain) were used to observe the MLG features on fracture surfaces (Hitachi S5200 microscope, Hitachi High–Technologies America Inc., USA) and to check the homogeneity of the distribution of the graphene nanosheets in the composites, as well as to characterize their ceramic grain morphology (FEI-Teneo microscope, Thermo Fisher, Cambridge, MA, USA). The MLG dispersion in the zirconia matrix was inspected on cross-sections polished up to 1 μm using backscattered electron (BSE) contrast. The polished cross-sections were thermally etched in air at 100 ºC below the sintering temperature for 20 min to reveal the ceramic grain boundaries. To characterize the ceramic grains, the mean equivalent plane diameter and its corresponding standard deviation were quantified.

ImageJ and OriginLab softwares were used to analyze more than 300 grains for each material to fit the grain size distributions to a lognormal distribution.

The DC electrical conductivity of the sintered composites was measured at room temperature in a two-point configuration in the direction parallel to the SPS pressing axis, $\sigma_{\parallel}$, in order to evaluate the percolation level of the MLG nanostructures. A Solartron equipment (SI 1287A model, Ametec Scientific Instruments, Berwyn, PA, EEUU, CITIUS) was employed using a potentiodynamic method in a range of 0 to 10 mV in steps of 0.1 mV. To perform the measurements, the parallel in-plane faces of the samples were coated with colloidal silver paste and the electrodes were subsequently annealed at 600 ° C for 30 min in argon flow.

2.3 Hydrothermal ageing method

Each sintered disk was cut into four pieces and polished to 1 μm-diamond paste to perform accelerated hydrothermal degradation experiments. The polished samples were kept in an autoclave with distilled water at 134 ºC under 2 bar steam pressure for increasing exposure times in order to achieve a complete transformation of the tetragonal phase into monoclinic. The complete ageing kinetics for the 3Y-TZP ceramic was also recorded to isolate the effect of the incorporation of MLG (type -FLG or e-GNP- and amount) on the hydrothermal ageing of zirconia.

The response to ageing degradation was evaluated by determining the fraction of monoclinic zirconia on the polished surface of the samples as a function of the ageing time. Each sample was examined by XRD before and after each exposure to moisture in autoclave, measuring the amount of tetragonal and monoclinic phase by recording the XRD patterns in a short 2θ range scanning from 27º to 33º with a step size of 0.015º and a time per step of 0.5 s. The monoclinic phase content V_m was calculated as described by Toraya *et al* [45]:

$$V_m = \frac{1.311\, X_m}{1 + 0.311\, X_m} \qquad (1)$$

evaluating the monoclinic/tetragonal ZrO_2 ratio, X_m, by the measurement of the area under the monoclinic and tetragonal main diffracted peaks registered in the XRD patterns using the Garvie and Nicholson equation [46]:

$$X_m = \frac{I_m\{\bar{1}\ 1\ 1\} + I_m\{1\ 1\ 1\}}{I_m\{\bar{1}\ 1\ 1\} + I_t\{1\ 0\ 1\} + I_m\{1\ 1\ 1\}} \qquad (2)$$

where $I_j\{h\ k\ l\}$ is the area of the $\{h\ k\ l\}$ diffraction peak of the j phase (m stands for monoclinic and t for tetragonal).

The transformation of metastable tetragonal ziconia to the monoclinic phase is governed by the nucleation and subsequent growth of the transformed monoclinic areas. The sigmoidal curves obtained by plotting the surface m-fraction versus ageing time are

commonly adjusted for a kinetic analysis using the Mehl-Avrami-Johnson formalism [47]:

$$f = \frac{V_m - V_0}{V_{max} - V_0} = 1 - \exp(-(bt)^n);\ b = b_0 \exp(-\frac{Q}{RT}) \qquad (3)$$

where V_m is the monoclinic phase content after ageing time t at absolute temperature T, V_0 and V_{max} are the initial and saturation contents of monoclinic phase, *b* is an Arrhenius thermally activation term (b_0 is constant, Q is the apparent activation energy, R is the ideal gas constant), and *n* is an exponent related to the nucleation and growth conditions of the monoclinic regions [48]. The activation energy values for ageing are between 40 and 120 kJ / mol and the exponent *n* is found in the literature in the range of values 0.5 to 4 [48]. Equation (3) can be rewritten as $\ln\left(\ln\left(\frac{1}{1-f}\right)\right) = nln(t) + nln(b)$, and the *n* and *b* values can be determined from the slope and intercept of the linear $\ln\left(\ln\left(\frac{1}{1-f}\right)\right)$*vs.* $\ln(t)$ plot. The ageing parameters *n* and *b* were estimated by fitting the experimental points using the least squares method for the FLG and e-GNP composites, as well as for the monolithic 3Y-TZP. The V_{max} values used to calculate f have been fixed in all the MAJ fits taking the value of the initial tetragonal fraction measured by XRD of each sintered material.

The propagation of the t- to m- transformation from the surface to the bulk was explored by SEM. The depth of the microcracking layer was inspected in the polished cross-sections of aged specimens after 10 h in autoclave for the 3Y-TZP and the FLG composites and after 24 h for the e-GNP composites. These ageing times were selected based on the monoclinic fraction achieved (~10–20%) after accelerated hydrothermal degradation tests.

Finally, a hydrothermal degradation test was performed for a 24 h ageing time in the case of the 2.5GNP and 2.5rGO composites to compare the ageing resistance between the composites prepared with different types of GBN.

3. RESULTS AND DISCUSSION

3.1 Microstructural characteristics of the zirconia/MLG composites

The density values of the as-sintered samples are shown in Table 2. Full densification was achieved for the monolithic zirconia and the composites prepared using e-GNP, validating the selected sintering conditions. In the case of the 3Y-TZP/FLG composites, highly dense materials have been obtained. A slight decrease in relative density has been observed in these composites with increasing FLG content, according to a previous report for similar SPSed composites prepared with higher FLG content (10 and 20% vol%) [49]. The authors attributed this effect to the existence of porosity between the graphene sheets, since no porosity was observed within the ceramic matrix. A decrease in relative density has also been reported in TZP composites that incorporate graphene nanoplatelets after

spark plasma sintering at 1350 ° C [21] and 1400 ° C [14]. Pores provide additional grain surfaces that can be exposed to water, and are therefore susceptible to spontaneous transformation. In conventionally sintered 3Y-TZP with grain sizes $\geq$ 350 nm, it is well known that porosity has a large effect in decreasing resistance to LTD, but this is not the case in 3Y-TZP with nanometric grain size (less than 200 nm) [50]. These authors have shown that spark plasma sintered 3Y-TZP with grain sizes $\leq$ 120 nm, even with connected porosity (very low relative density $\sim$ 90%), are highly resistant to hydrothermal degradation [50].

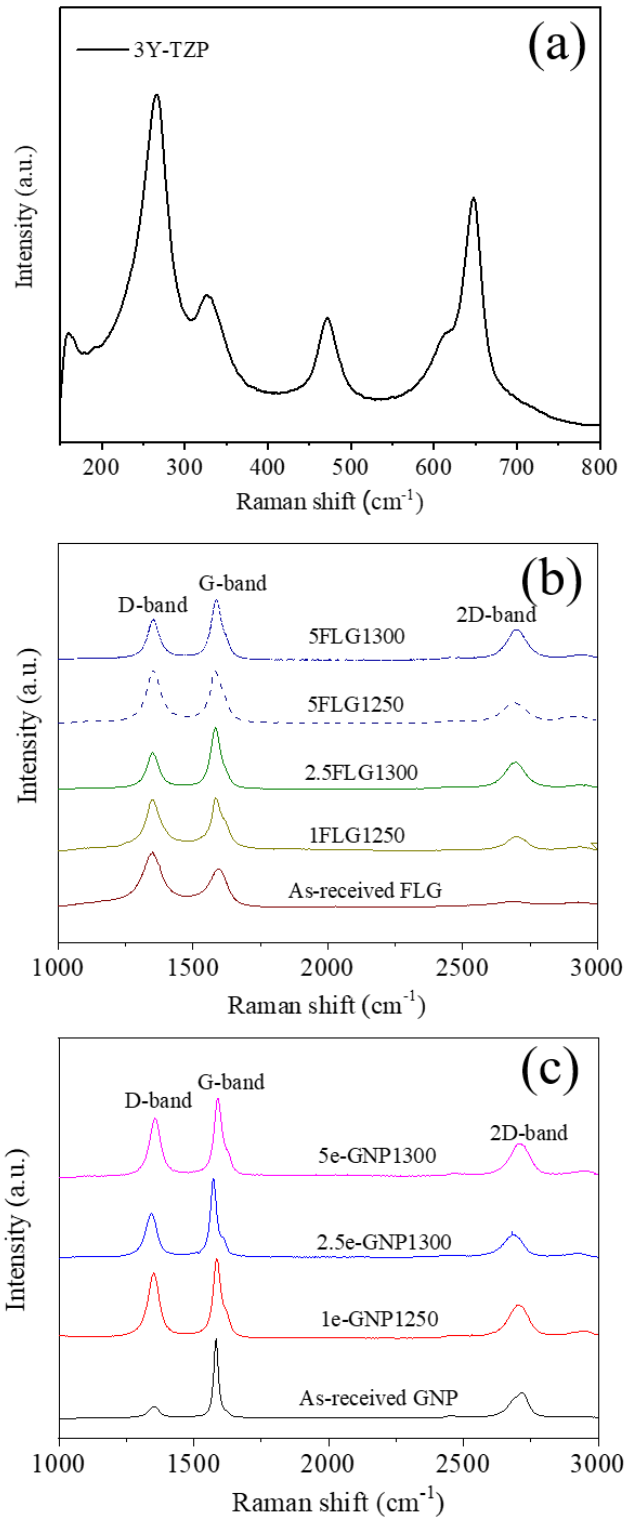

Figure 1. Raman spectra of the fracture surfaces corresponding to a) 3Y-TZP1250, b) 3Y-TZP/FLG and c) 3Y-TZP/e-GNP composites. Raman spectra of the as-received FLG and GNP powders are also included for comparison.

Figure 1 collects the Raman spectra of the sintered composites and the monolithic 3Y-TZP ceramic. In Fig. 1a the six theoretically predicted Raman bands for tetragonal

zirconia at 160, 266, 327, 470, 612 and 647 cm^{-1} are clearly observed, confirming that the tetragonal phase is the main one in the ceramic. The characteristic peaks of the graphitic structures are clearly observed in the spectra of the composites (Figures 1b and 1c): the D-band (~1350 cm^{-1}), the G-band (~1580 cm^{-1}) and the 2D-band (~2700 cm^{-1}). The presence of these bands confirms the preservation of the bidimensional graphene-based nanostructures in the composites after the powder processing and sintering. Data for the intensity ratios I_D/I_G and I_{2D}/I_G (calculated by means of integrated areas) for the sintered composites with FLG and e-GNP are presented in Table 3.

Table 2. Relative density, zirconia mean grain size and crystallographic phase quantification of as-sintered materials.

Material	Density (%)	Grain size (nm) ± s.d.	T content (%)	C content (%)	M content (%)
3Y-TZP1250	100	230 ± 130	93.9 ± 0.3	4.16 ± 0.13	1.9 ± 0.2
1FLG1250	98.8	280 ± 160	94.5 ± 0.3	3.59 ± 0.13	2.5 ± 0.2
1e-GNP1250	99.6	190 ± 100	94.5 ± 0.3	3.0 ± 0.2	2.5 ± 0.2
2.5FLG1300	98.9	460 ± 130	93.0 ± 0.3	5.11 ± 0.14	1.9 ± 0.3
2.5e-GNP1300	99.6	250 ± 110	92.4 ± 0.3	5.4 ± 0.3	2.2 ± 0.2
5FLG1250	96.9	240 ± 100	94.8 ± 0.4	2.9 ± 0.3	2.4 ± 0.2
5FLG1300	97.6	330 ± 190	93.7 ± 0.3	4.04 ± 0.14	2.3 ± 0.3
5e-GNP1300	100	230 ± 120	93.2 ± 0.2	4.28 ± 0.12	2.6 ± 0.2

A drastic increase in the I_D/I_G ratio is observed for the e-GNP composites after processing and sintering compared to the corresponding value for the as-received GNP (0.33 ± 0.09 [38]). On the contrary, a decrease in this ratio is observed in the FLG composites compared to the value of the as-received FLG (2.33 ± 0.04 [42]). This remarkable difference is closely related to the different processing routines used to prepare the two different types of composites. Usually, the I_D/I_G intensity ratio is indicative of the presence of defects on the structure of graphitic materials. However, this ratio is also related to the in-plane GNP size as the GNP borders are detected as defects by Raman spectroscopy [51,52]. In this context, the drastic increase in the I_D/I_G ratio in e-GNP composites compared to this ratio for as-received GNP can be related to a reduction in the lateral size of e-GNP due to the fracture of the nanoplatelets caused by high-energy milling, as previously reported [38]. On the contrary, the observed I_D/I_G decrease in the FLG composites with respect to the as-received FLG is not related to a reduction in the lateral size of the FLG due to the powder processing routine (not as energetic as the high-energy planetary ball milling) but rather to the sintering process. Although the as-received FLG presents an I_D/I_G value similar to the published one for defective graphene nanosheets [53], the sintering process promotes a restoration of the graphene structure, resulting in a lower number of defects and a higher crystallinity in the FLG in sintered composites [38,42,53,54].

The I_{2D}/I_G ratio is also indicative of the quality of the structure of the graphene network [55]. All sintered 3Y-TZP/e-GNP composites have I_{2D} / I_G values (Table 3) slightly lower than the one corresponding to the as-received GNP (1.08 ± 0.05 [38]), revealing that the crystallinity of the nanoplatelets has not been significantly damaged during the sintering process. On the other hand, an increase in the I_{2D}/I_G ratio is observed in sintered 3Y-TZP/FLG composites compared to the as-received FLG (0.434 ± 0.015 [42]), confirming the restoration of the graphene structure during the high temperature process. The highest I_{2D}/I_G values for the FLG composites are obtained for those sintered at 1300 ° C, as a consequence of the improved crystallinity in these composites after sintering at a higher temperature [42].

Table 3. Intensity ratios of the D and 2D bands with respect to the G peak of Raman spectra, electrical conductivity, and ageing parameters obtained for the sintered composites. The ageing parameters of the reference material are also included for the sake of comparison.

Material	I_D/I_G	I_{2D}/I_G	σ ($S \cdot m^{-1}$)	n	b (h^{-1})
3Y-TZP1250			-	1.46(9)	0.0190(3)
1FLG1250	0.95(7)7	0.47(8)	-	1.60(11)	0.00832(10)
1e-GNP1250	1.24(6) **	0.934(19)**	-	1.12(6)	0.0003516(19)
2.5FLG1300	1.21(4)*	0.93(5)*	3.06(5)*	1.31(6)	0.02046(24)
2.5e-GNP1300	1.07(11)	0.88(8)	-	1.025(12)	0.003652(7)
5FLG1250	1.42(9)*	0.56(4)*	20.9(7)*	1.92(18)	0.01134(23)
5FLG1300	1.30(3)*	0.77(6)*	73.9(1.7)*	1.40(10)	0.0560(14)
5e-GNP1300	1.05(5)	0.93(5)	12.3(7)	1.60(11)	0.0184(3)

*From Ref. [42]

**From Ref. [38]

For both e-GNP and FLG composites, the 2D band fit could be performed using three Lorentz functions [38,42] (deconvolutions of the 2D band for the 2.5e-GNP1300 and 1FLG1250 composites are presented in the Fig. 1 in the Supplementary Section, as an example). According to previous authors [56,57], this reveals that both nanostructures present a number of layers lower than 10. Thus, in the case of 3Y-TZP/e-GNP composites, the Raman analysis confirms that the planetary ball milling under dry conditions produced severe exfoliation of the GNP, as referred to in [38].

Figure 2 illustrates the morphology of the different multilayered graphene fillers observed on the fracture surfaces of the composites with 5 vol% MLG content. The FLGs (arrowed in Fig. 2a) look transparent and wavy, coating extense zirconia areas due to their large lateral size. In contrast, e-GNP (arrowed in Fig. 2b) have a sub-micrometer lateral size, confirming the severe reduction in the lateral dimension of the platelets achieved by planetary ball milling in dry conditions, in agreement with the Raman analysis. The flatness of the e-GNP arranged as rigid nanoplatelets between the ceramic grains contrasts with the wavy look exhibited by the FLG, which smoothly wraps up clusters of zirconia grains (Fig. 2a).

The good dispersion of the MLG in their respective sintered composites was confirmed by SEM inspection in BSE mode. A homogeneous distribution of the graphene nanosheets (dark phase) through the ceramic matrix (bright), regardless of the content and MLG used, was found in all composites (Figure 3). The FLG were preferentially oriented with their ab planes aligned perpendicular to the SPS pressure axis (Fig. 3a and Fig. 3c), while the e-GNP were isotropically oriented surrounding small zirconia zones in the 3Y-TZP/e-GNP composites (Fig. 3b and Fig. 3d). The improvement in the MLG dispersion was noticeable in the composites processed using planetary ball milling, giving place to finely dispersed e-GNP between the zirconia matrix grains. In the case of the 3Y-TZP/FLG composites, small interface gaps between FLG sheets have been observed at high magnification (not shown), which is consistent with the decreasing trend found in relative density values (Table 2) as indicated by Muñoz Ferreiro *et al.* [49] and Obradovick and Kern [21].

In relation to the matrix, all the composites exhibited sub-micrometric equiaxed zirconia grains as reported elsewhere [38,49,58]. Table 2 shows the mean grain size and standard deviation of the lognormal distribution of the ceramic grains. Fine-grained microstructures have been achieved in all 3Y-TZP/MLG composites regardless of the processing conditions used and the volume fraction of the filler incorporated without a significant decrease in ceramic grain size compared to the monolithic zirconia, as usually reported with GBN incorporation [13,16,18]. Matrix coarsening and a more heterogeneous ceramic grain distribution are observed in the 3Y-TZP/FLG composites sintered at 1300 ° C, i. e., in the 2.5FLG1300 and 5FLG1300 composites. This coarsening effect is less severe in the case of a 5 vol% FLG addition, in agreement with its lower relative density. The 3Y-TZP/e-GNP composites show matrix microstructures similar to the monolithic zirconia, except in the case of the 1e-GNP1250 composite. The addition of 1 vol% e-GNP favors a slight grain refinement as well as a more homogeneous grain size distribution. It is widely accepted that the dependence of hydrothermal degradation with increasing grain size is to increase transformability of the tetragonal grains (as it is well-established in the 3Y-TZP toughening transformation). Therefore, coarsed tetragonal grains are more transformable and the increase of the grain size leads to a faster degradation.

The matrices mainly consist of reduced tetragonal zirconia phase ($ZrO_{1.95}$) (JCPDS 01-081-1544) in all the composites. A partial reduction of the zirconia matrix is achieved during the sintering process due to the highly reducing graphite mold and vacuum conditions used in the SPS [18,40,59]. A higher content of oxygen vacancies is created by reducing the partial oxygen pressure when 3Y-TZP samples are sintered under reducing conditions rather than in an air atmosphere. Reduced zirconia samples with density and average grain size values similar to air-sintered samples degrade significantly faster, as the vacancy diffusion rate that governs the spontaneous transformation from the tetragonal to the monoclinic phase increases [60,61].

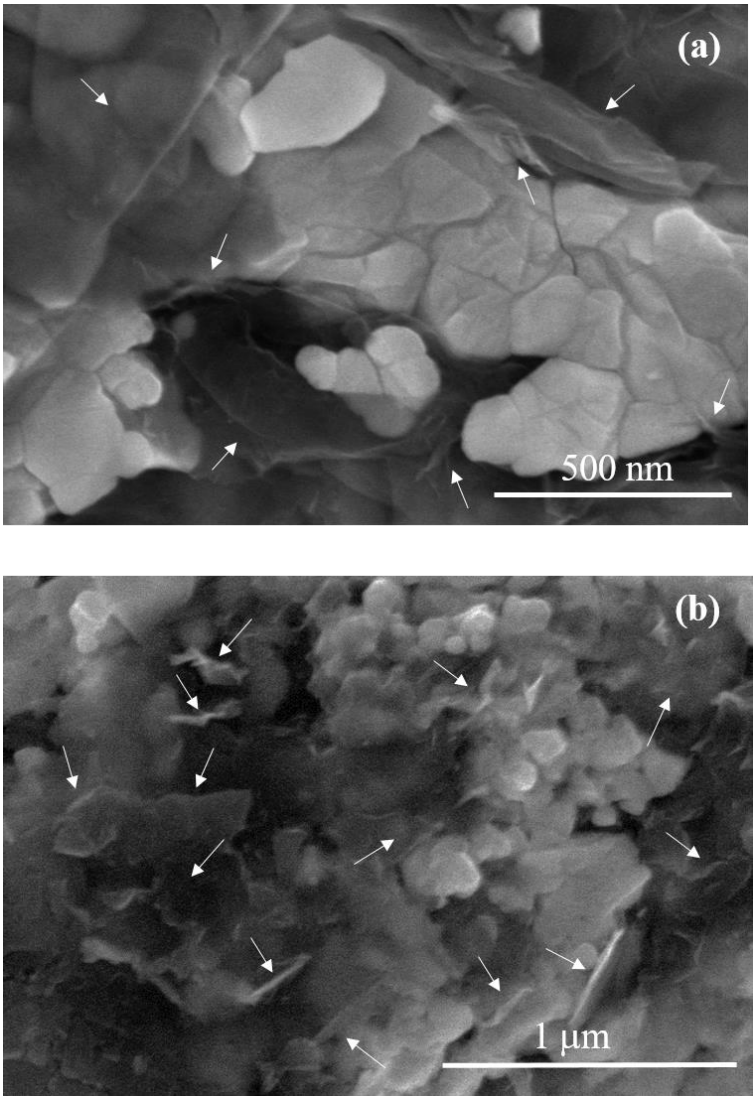

Figure 2. SEM images of the fracture surfaces of the a) 5FLG and b) 5e-GNP composites. Multilayered graphene nanostructures are indicated by arrows in the micrographs.

Table 2 collects the quantification of Rietveld refinement of the cubic (C), tetragonal (T), and monoclinic (M) zirconia phases present in the as-sintered materials. All the as-SPSed samples have similar cubic (~3-6%), tetragonal (~92-95%) and monoclinic (~2%) zirconia contents regardless of the MLG type incorporated into zirconia and the processing conditions used. The increasing addition of FLG or e-GNP does not affect the percentage of zirconia phases either. The initial content of the zirconia phases is relevant in the ageing response, since it influences the maximum quantity of the tetragonal phase susceptible to transformation into monoclinic. Furthermore, the proportion of the initial cubic phase also influences the ageing process, making neighboring tetragonal grains more susceptible to transform into the monoclinic phase [62].

In view of the similar values of density, grain size and initial zirconia phases fraction attained in most of the as-sintered 3Y-TZP/MLG composites in comparison to the monolithic 3Y-TZP sample (Table 2), the intrinsic effect of the graphene incorporation on LTD kinetics can be inferred in these composites.

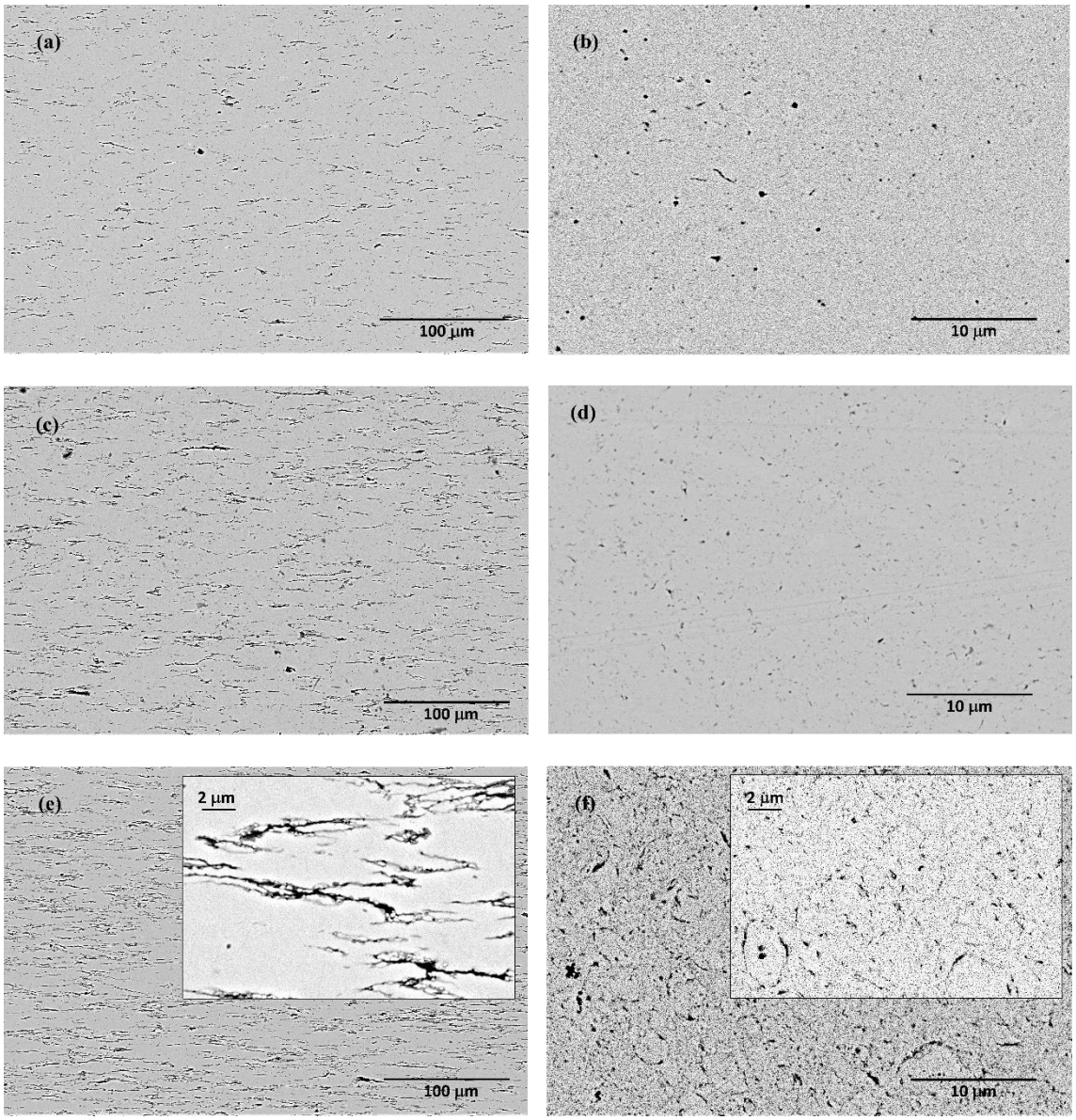

Figure 3. BSE-SEM images illustrating the distribution of the graphene nanostructures in the cross-section of a) 1FLG1250, b)1e-GNP1250, c) 2.5FLG1300, d) 2.5e-GNP1300, e) 5FLG1300 and f) 5e-GNP1300 composites. Figures e) and f) include an enlarged view to show in detail the degree of dispersion achieved for the graphene nanosheets in the composites.

3.2 Hydrothermal degradation behavior of the 3Y-TZP/MLG composites

The monoclinic zirconia fraction V_m plotted as a function of the hydrothermal ageing time (Figure 4) shows a sigmoidal increase both in the monolithic zirconia and in the MLG composites.

Fig. 4a shows the ageing curves of all the FLG composites, showing that the 1FLG1250 and 5FLG1250 composites exhibit a similar enhanced ageing resistance compared to the

monolithic zirconia, while the 2.5FLG1300 composite behaves similarly to the zirconia reference sample and the 5FLG1300 composite degrades faster than zirconia.

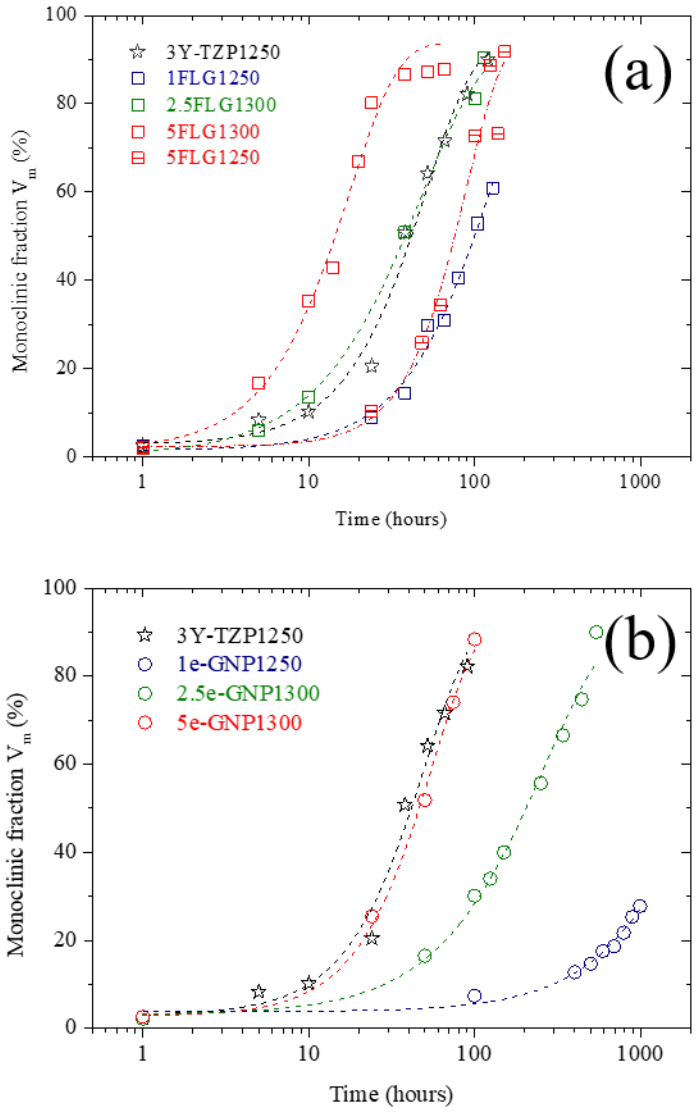

Figure 4. Ageing curves of the 3Y-TZP/MLG materials: a) FLG and b) e-GNP composites. The LTD curve of the monolithic zirconia is included in the plots to facilitate comparison.

The 1FLG1250 composite ageing response indicates that this small FLG addition (1 vol%) significantly delays the hydrothermal degradation. The main microstructural differences in this composite compared to the 3Y-TZP1250 material are the mean grain size value of the matrix, slightly larger in the composite, and that elongated graphene nanosheets, mainly oriented parallel to the surface of the sample in contact with water, are wrapping zirconia grain clusters. As the effect of the increase of grain size is the promotion of the zirconia ageing at 134 ºC [63], the enhancement of the zirconia ageing resistance in this composite is a clear effect of the FLG filler arranged between the zirconia grains.

The matrix microstructure of the FLG composites sintered at 1300 ° C differs mainly in two characteristics: mean grain size and degree of reduction. As it has been mentioned above, the sintering of the 3Y-TZP/MLG composites in reducing conditions due to the graphite mold and vacuum conditions used during the SPS process promotes the reduction of the zirconia matrix. Moreover, previous studies [59] have revealed that a stronger reduction of the zirconia matrix results after sintering at 1300 ºC compared to the reduction degree attained at a lower SPS temperature. This resulted even in a remarkably different electrical behavior in the two ceramics as a consequence of the different number of oxygen vacancies and inyected electrons in the ceramics with different reduction level. The reduction in zirconia ceramics contributes to the acceleration of the moisture-driven tetragonal to monoclinic transformation [3,60,61], as well as the larger grain size also increases LTD, so the influence of the FLG content on improving the ageing behavior of the composites can be reasonably inferred from the experimental LTD curves in Fig. 4a.

The 2.5FLG1300 composite maintains the ageing rate of monolithic zirconia, even having a coarse microstructure (twice the grain size) and a higher degree of reduction than the 3Y-TZP1250 reference material, so it can be noted that a 2.5 vol% FLG addition is also favorable to restrict ageing.

In the case of 5 vol% FLG addition, very different ageing rates have been found in the composites sintered at different temperatures. In view of the ageing kinetics of the 5FLG1250 and 5FLG1300 composites (Fig. 4a), it can be assured that the degree of reduction in the zirconia matrix plays a critical role in the t-m transformation of these composites. Comparing their LTD, the moisture-driven transformation rate in the 5FLG1250 composite is slower than in the 3Y-TZP1250 ceramic, while exhibiting similar grain size and slightly higher porosity, which supports the beneficial effect of the FLG incorporation delaying the hydrothermal degradation in the composites. Concerning porosity, although in conventional 3Y-TZP it is well known that porosity has a large effect on decreasing resistance to LTD, this is not the case in SPS samples with grain sizes below 300 nm [50].

The hydrothermal ageing in the 5FLG1300 composite was expected to be slower than in the 2.5FLG1300 according to its different grain sizes (330 and 460 nm, Table 2). However, its faster ageing response suggests that the increasing amount of FLG incorporated into zirconia is influencing the ageing kinetics in a detrimental way. It is plausible that the presence of homogeneously distributed graphene nanosheets also contributes to increasing the reduction level in the zirconia composites, as they are graphitic nanostructures. It is very likely that the increase in FLG content leads to further reduction of the matrix through the connection of the MLG percolated network and the surrounding graphite mold during the SPS process. To elucidate the degree of percolation of the graphene network in the composites, electrical conductivity data were obtained for the composites (Table 3). As it can be observed, a non-negligible electrical conductivity could be measured for the composites with 2.5 and 5 vol% FLG. This reveals that the percolation limit is between 1 and 2.5 vol% for the FLG composites. Furthermore, significantly higher conductivity was obtained for the 5FLG1300 composite. Thus, it can

be assured that a totally percolated graphene network is distributed throughout the zirconia matrix in this conductive composite, which could induce a higher reduction of the matrix.

The similar ageing kinetics observed in the 1FLG1250 and 5FLG1250 composites, taking into account their different grain sizes (Table 2), agree with the proposal of acceleration of LTD by zirconia reduction promoted by the highly percolated network achieved in 5FLG1250 (Table 3). It is interesting to note that a decrease of 50 ° C in the SPS temperature significantly affects the grain size and the level of zirconia reduction in the composites with the addition of 5 vol% FLG. The 5FLG1250 composite underwent a notable decrease in the t-m transformation rate, comparable to the 1FLG1250.

Clearly, the presence of FLG between the zirconia grains delays the hydrothermal degradation. The effect of FLG can be twofold: on the one hand, it can modify grain boundaries and give rise to residual stresses that can affect transformability in Y-TZP grains [64] and, on the other hand, it can be expected to provide an intrinsic contribution associated with its impermeable nature [23].

Concerning the effects of FLG on zirconia grains and grain boundaries, crystalline and amorphous zirconia/graphene interfaces have been shown to coexist in FLG composites with a 10% FLG content and an intermediate zirconia oxycarbide has been detected in some grain boundaries [49], which could favor resistance to ageing. Although it has been reported that the incorporation of graphene favors the transformation from tetragonal to monoclinic in fine zirconia powder [65], both the presence of a vitreous phase, leading to grains with more rounded shapes, and the incorporation of carbon atoms in the zirconia lattice structure diminish the transformability of the tetragonal zirconia grains [66] and could delay the ageing response. Regarding the role of residual stresses, the FLG incorporation does not appear to play a favorable role in delaying the LTD of these composites. Recently, the Raman spectra of these FLG composites have been analyzed in depth in [42] showing that the positions of the G and 2D bands are shifted to higher frequencies compared to the as-received FLG as a consequence of the residual stresses imposed by the ceramic matrix, as suggested by previous studies [18,67]. Androulidakis et al. [68] reported a frequency shift to higher value for the 2D band of few layer graphene under compressive deformation. Therefore, if FLG is in compression in 3Y-TZP/FLG composites, the zirconia grains are in traction and, therefore, the transformability of t-ZrO_2 is enhanced [64]. Thus, the composites would be more susceptible to undergo hydrothermal ageing.

In relation to the intrinsic contribution of FLG on ageing, it is expected that the distribution of these graphene nanosheets throughout the matrix will block the water vapor transport. The rGO was demonstrated to be highly impermeable to moisture, and the incorporation of graphene flakes has been shown to effectively prevent the penetration of moisture into polymers, metals, and ceramic materials [28–36]. Since FLGs are mainly arranged with their main ab plane parallel to the surface exposed to moisture, they seem also to be effective as moisture barriers in zirconia composites, acting as a water vapor

diffusion barrier preventing the contact of the zirconia grain clusters with water species and, therefore, delaying the hydrothermal degradation in the composites.

The ageing curves of the 3Y-TZP/e-GNP composites (Fig. 4b) clearly show that the addition of e-GNP strongly influences the hydrothermal degradation of zirconia. It is noteworthy that for all the e-GNP contents considered here, the addition of e-GNP restricts the t-m transformation compared to the monolithic zirconia. However, the higher the e-GNP content, the less effective it will be to improve ageing resistance. The 1e-GNP1250 composite exhibits remarkable resistance to hydrothermal degradation: while the monoclinic content of the 1e-GNP1250 composite did not practically increase after 100 h in autoclave, the initial tetragonal zirconia content was completely transformed into monoclinic in the 3Y-TZP1250 sample. The outstanding restriction to ageing detected for the 1e-GNP1250 composite (far from saturation after 1000 h ageing) can be related to the very fine grain size achieved for this material (190 nm), but it could also be favored by the effect of the e-GNP finely dispersed between the zirconia grains in the same line discussed above for the FLG composites. The delay in hydrothermal degradation with grain refinement has been widely reported [3,4,69–71]. Eichler et al. [71] have studied the hydrothermal degradation of 3Y-TZP with grain sizes in the range of 110-480 nm and only in samples with grain sizes larger than 210 nm significant amounts of monoclinic phase were formed by degradation at 200 ° C for 6 h in an autoclave. LTD experiments carried out at 131 ° C for 60 hours in 3Y-TZP sintered by SPS showed no phase transformation in samples with low density and small grain size (< 200 nm) [50]. Garmendia *et* al. [6] also described an elevated LTD resistance in spark plasma sintered 3Y-TZP reinforced with carbon nanotubes attributed to the fine ceramic grain size (below 220 nm) attained by SPS.

The favorable effect of the addition of e-GNP on hydrothermal degradation can be inferred by comparing the LTD curves of the 2.5e-GNP1300 and 5e-GNP1300 composites, both with better resistance to LTD than the monolithic zirconia and with matrix microstructures similar to 3Y-TZP1250 in density, grain size, and initial zirconia phase content. The incorporation of increasing amounts of e-GNP above 1 vol% clearly accelerates hydrothermal degradation with respect to the 1e-GNP1250 composite, which could be related to the higher degree of 3Y-TZP reduction achieved as a result of sintering at 1300 ° C and the greater connectivity between nanosheets of the e-GNP network. Electrical conductivity measurements (Table 3) revealed that the percolation limit is between 2.5 and 5 vol% for the e-GNP composites and the e-GNP network is totally percolated in the conductive 5e-GNP composite. However, even for the addition of 5 vol% of e-GNP, resistance to hydrothermal degradation is slightly favored compared to that of monolithic zirconia.

Although in polymeric composites extense FLG have been shown to be more efficient as vapor barriers when arranged with their main plane parallel to the surface exposed to water [28], in this study a stronger decrease in the ageing rate is observed in the 3Y-TZP composites that incorporate e-GNP (randomly oriented) compared to the FLG composites. Since the e-GNP nanostructures are very finely dispersed, the proportion of

these submicrometer-sized nanosheets between zirconia grains is much higher than that achieved with extense FLG considering similar vol% addition. Thus, a significant number of them are also oriented so that their main ab plane is preventing the diffusion of water-derived species through them. Therefore, the fine e-GNP sheets could advantageously reduce the contact between zirconia grains and consequently, the impermeability of the e-GNP could contribute to limiting the propagation of the t-m transformation into the composite bulk in a more effective way.

An enhancement of the ageing resistance would be expected with the increase in the MLG located between the ceramic grains taking into account the intrinsic effect of the MLG, since it improves the moisture barrier effect as well as shuts off the propagation of the transformation t-m from one zirconia grain to the next. However, the proneness to ageing of the composites sintered at 1300 ° C increases with the increase in the MLG content. A higher concentration of electrons and oxygen vacancies in 3Y-TZP/MLG composites when increasing the MLG content and the sintering temperature, both contribute to the acceleration of moisture-driven monoclinic transformation [3,60,61]. Bartolomé *et al.* [60] found that 3Y-TZP ceramics sintered in an atmosphere of argon/hydrogen at 1430 ° C for 2 h exhibited a significantly faster transformation to monoclinic under LTD compared to similar samples sintered in air. The oxygen vacancies introduced by reducing the partial oxygen pressure explained the increase in the ageing rate observed in reduced zirconia [60]. Ubenthiran *et al.* [61] also attributed the rapid phase transformation in argon-sintered samples at 1450 and 1500 ° C to the increase in structural vacancies due to oxygen-free sintering. Chevalier *et al.* [3] pointed out that the accelerated LTD observed in the previous work [60] was more likely related to the increase in the electron concentration as responsible for the increase in hydrogen transport and H_2O permeation in the zirconia lattice. Therefore, the detrimental effect of a more reduced matrix with increase in MLG content counterbalances the benefits of the intrinsic effect of MLG as moisture barrier.

It is worth highlighting as a remarkable point of this study that a low monoclinic fraction (below 10% after 5 h in water vapor at 134 ºC) is retained in all composites (except for the 5FLG1300 composite), which opens the door for them to be considered suitable for implants, at least with regard to this requirement established in ISO 13356 [72].

3.3 Ageing performance of zirconia/graphene-based nanostructure composites as biomaterials

The kinetic parameters *n* and *b* in the Mehl-Avrami-Johnson (MAJ) equation were determined by linear fitting of the corresponding plots of $\ln\left(\ln\left(\frac{1}{1-f}\right)\right)$ *vs.* $\ln(t)$ presented in Figure 5. The linear plots (Fig. 5) show similar slopes for 3Y-TZP and most of the 3Y-TZP/MLG composites. Table III collects values of *n* and *b* useful for predicting the ageing kinetics of the composites exposed to moisture at 134 °C.

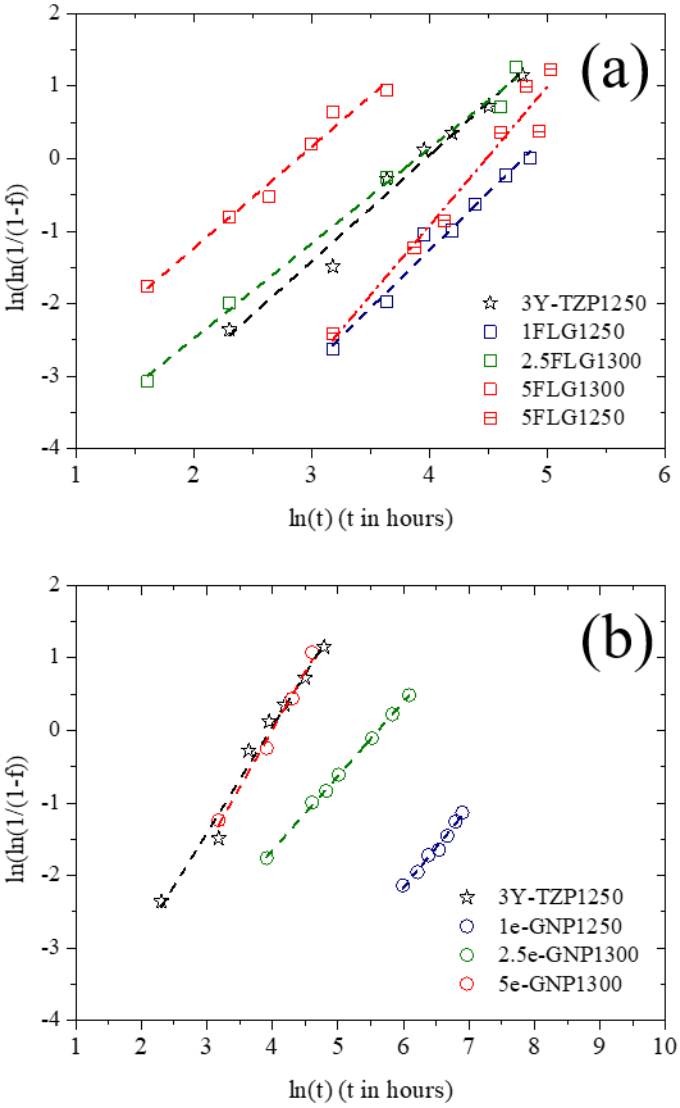

Figure 5. Linear fittings of experimental data to determine the ageing parameters for a) FLG and b) e-GNP composites.

A value of n≅1.5 is obtained for the 3Y-TZP1250 ceramic, 1FLG1250, 2.5FLG1300, 5FLG1300 and 5e-GNP1300 composites, regardless the MLG type and content, grain size, degree of matrix reduction or relative density. The 1e-GNP1250 and 2.5e-GNP1300 composites exhibit a lower n value (≅ 1.0) and, contrarily, the 5FLG1250 composite exhibits a higher n value (≅ 1.9). All these exponents are in the values range of 0.5-4 reported for yttria-doped zirconia materials [48]. Recently, Wei and Gremillard [63] analyzed the values of n found in the literature for yttria-doped zirconia ceramics and no dependence on the grain size, the amount of yttrium in the tetragonal phase or the proportion of cubic phase was found.

The onset of ageing is correlated to both n and b values (if n ≤1 the transformation starts immediately and if n > 1, then the onset of the transformation is delayed and for a given b value, the delay is more noticeable as n increases). The value of the b-parameter is

similar in the reference zirconia (b ≅0.02 h^{-1}) and in the 2.5FLG1300 and 5e-GNP1300 composites, in accordance with their similar LTD curves (Fig. 4) as they also have similar n values; instead, the onset of ageing is delayed in the 1FLG1250 composite since its b value is lower. The zirconia composites with 5 vol% FLG present a noticeable difference in their b values, much lower in the 5FLG1250 case while its n value is higher compared to 5FLG1300 one, so the LTD onset is delayed in these composites when a lower sintering temperature is used in SPS and these different values of the kinetic parameters support the higher ageing resistance exhibited by the 5FLG1250 composite (Fig. 4a). The increase of b-values from 0.00035 to 0.018 h^{-1} with increasing e-GNP content are also in agreement with the favored degradation found in the 3Y-TZP/e-GNP composites (Fig. 4b). The dependence of the ageing onset with n and b values has been observed in many 3Y-TZP materials prepared with different processing routes and tested under different ageing conditions [63].

The propagation of the t-m transformation from the surface in contact to water vapor towards the material bulk has been explored by SEM inspection of the damaged-zone depths in both sets of 3YTZP/MLG composites as well as in the monolithic zirconia. Images have been acquired in case of the 3Y-TZP1250 and the FLG composites after 10 h under ageing conditions and in the e-GNP composites after 24 h ageing, since these latter ones exhibited enhanced ageing resistance. The micro-cracked region developed close to the sample surfaces exposed to water, related to the advance of the transformation front, is clearly observed in the monolithic zirconia (∼ 8 μm-depth) and also, but much smaller, in the e-GNP composites (∼1-2 μm-depth) except for 1e-GNP1250, in which it has not developed as it has not undergone ageing after 24 h in autoclave. In the case of the 3Y-TZP/FLG composites, no microcracks are observed in any sample although the amount of transformed zirconia after 10 h ageing is quite similar to the one in 3Y-TZP1250 or even superior in the case of the 5FLG1300 composite (Fig. 4). The 3Y-TZP/MLG composites retain the structural integrity better than the monolithic zirconia, so the ageing effect on the mechanical properties is expected to be less severe.

Figure 6 shows the BSE-SEM images of the polished cross-sections of the aged 3Y-TZP1250 ceramic and 2.5FLG1300 and 2.5e-GNP1300 composites to illustrate the comparison of the microstructural damage developed. A damaged zone is clearly distinguished close to the surface exposed to water (at the top of the micrographs) in the zirconia reference material as well as in the 2.5e-GNP1300 composite (Fig. 6a and Fig. 6c). The microcracks generated by the volumen change associated to the tetragonal to monoclinic transformation have been filled by the resin (gray color, at the top of Fig. 6a and Fig. 6c) used for preserving the eventual damaged zone during polishing. The damaged zones are well-delimited and extend throughout the region in contact to water with a wider layer in the 3Y-TZP1250 material than in the 2.5e-GNP1300 composite. The damaged zone observed in 5e-GNP1300 (not shown) is similar to the one in 2.5e-GNP1300, also restricted to 1-2 μm-depth. Since 24 h-aged 5e-GNP1300 had a higher monoclinic zirconia fraction than 10 h-aged zirconia, the less extended damaged layer in the composite than in zirconia suggests that the extent of microcracking does not increase as the transformation zone grows with the addition of e-GNP.

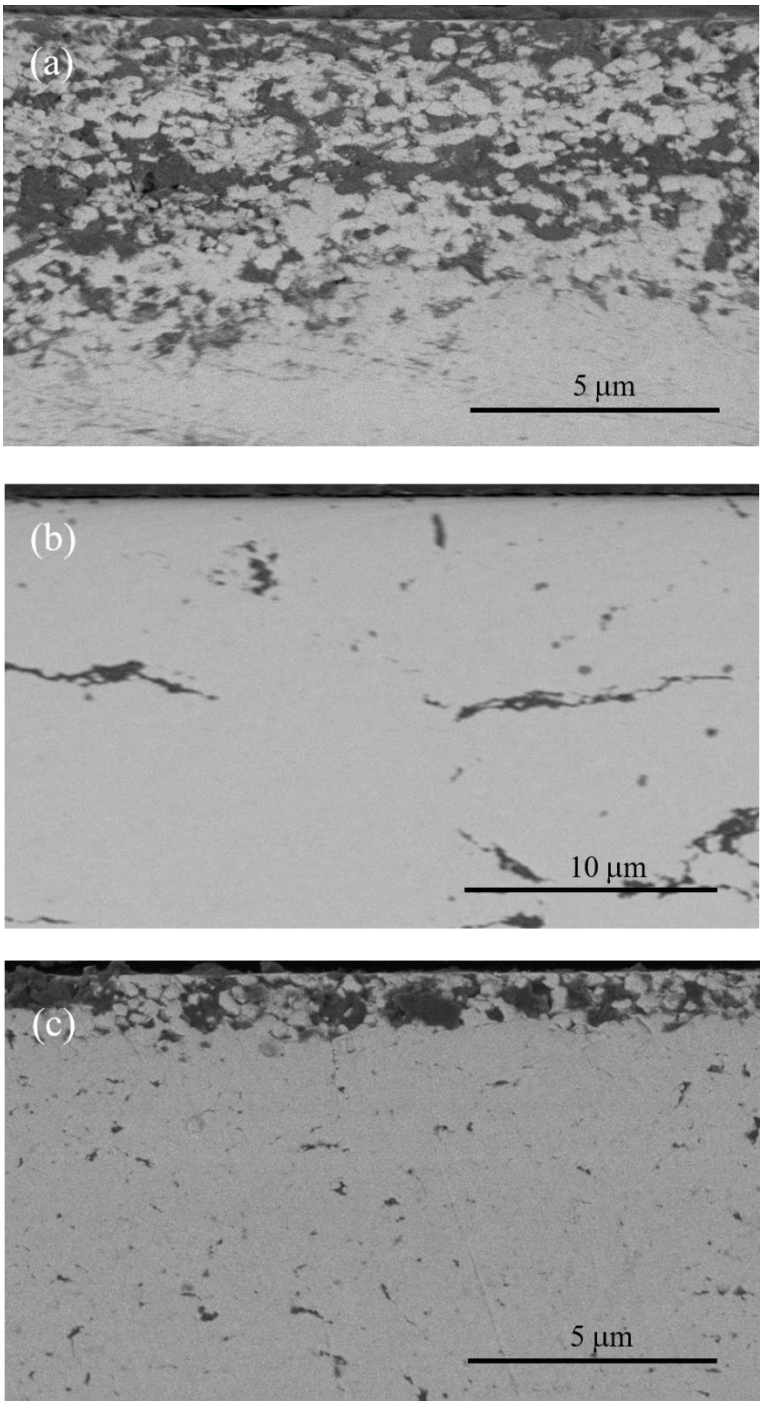

Figure 6. SEM images in BSE mode of cross-sections of aged materials: a) 3Y-TZP1250, b) 2.5FLG1300 and c) 2.5e-GNP1300 composite.

A superior microstructural integrity is observed in the 3Y-TZP/FLG composites, which have not developed damage after ageing. Figure 6b illustrates the appearance of the zone close to the surface exposed to water in 10 h-aged 2.5FLG1300 composite showing the FLG distribution over the composite cross-section, exclusively. Despite the fact that the 10 h-aged 2.5FLG1300 composite presents an amount of monoclinic phase fraction similar to 3Y-TZP1250 and the monoclinic content of 10 h-aged 5FLG1300 composite is

even higher, no sign of damage is appreciated in any of them. The absence of damaged zone indicates that the network of FLG homogeneusly distributed through the ceramic matriz confers an enhanced structural integrity to these composites, possibly by accommodating the volume change associated to the t–m transformation and, therefore, preventing microcracks.

Finally, the effect of the different GBN fillers (e-GNP, FLG, GNP and rGO) on zirconia ageing resistance is compared in Figure 7. The use of thick GNP nanostructures seems not to be favorable to delay LTD in zirconia as the amount of monoclinic phase developed in the 2.5GNP composite after 24 h in autoclave exceeds that of the monolithic sample, which disagrees with the qualitative estimations reported in [14]. The monoclinic content in the composites incorporating e-GNP, FLG or rGO nanostructures after ageing for 24 h is considerably lower than the measured one in monolithic zirconia. This result indicates that rGO is potentially very effective also in restricting the ageing-induced t-m transformation, in contrast with the accelerated LTD trend found when GO is added to air-sintered zirconia [73]. Furthermore, the 1FLG1250 and 2.5e-GNP1300 composites are very attractive since they exhibit similar LTD restriction than the 2.5rGO one with a lower FLG amount or with e-GNP obtained from cost-effective GNP. The low amount of monoclinic phase developed after ageing in the composites with thin GBN (below 10 graphene layers) analyzed in the present study makes these novel materials promising ageing resistant candidates for biomedical zirconia applications.

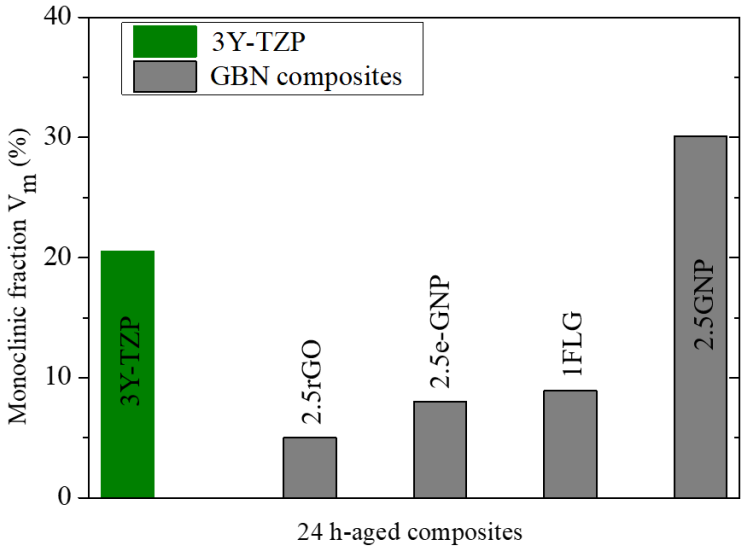

Figure 7. Comparison of monoclinic content in 3Y-TZP (as reference material) and in four different 3Y-TZP/GBN composites after 24 h in autoclave at 134 ºC.

4. CONCLUSIONS

The study of two sets of highly-dense 3Y-TZP composites incorporating two different bidimensional graphene-based nanostructures (commercial FLG and exfoliated GNP) in

different contents (1, 2.5 and 5 vol%), carried out with the aim of elucidating the effect of graphene as moisture barrier in the low-temperature hydrothermal degradation of zirconia, leads to the following conclusions:

- The favorable effect of the multilayered graphene addition restricting the moisture-driven t-m transformation in zirconia has been corroborated. The retarding of the ageing degradation was more noticeable in the case of e-GNP addition to 3Y-TZP than in the case of FLG addition, related to its finer dispersion and size.

- The MLG incorporation has effectively reduced the grain pullout and microcracking associated to zirconia LTD. A superior microstructural integrity was observed in the case of FLG addition.

- Most of the 3Y-TZP/MLG composites fullfilled the requirement of monoclinic fraction below 10% after 5 h in water vapor at 134 ºC established by the standard ISO 13356 to be considered suitable for implants.

The effect of the MLG addition retarding the ageing degradation as well as inhibiting damage and microcracking in the composites surface grants the enhanced structural performance of these novel composites of biomedical-grade 3Y-TZP with multilayered graphene for use as biomaterials.

ACKNOWLEDGEMENTS

This research was supported by the Ministerio de Ciencia, Innovación y Universidades (MCIU) under the project PGC 2018-101377-B-100 (MCIU/AEI/FEDER, UE) and by the Universidad de Sevilla (US) under the contract 2018/00000663 VI PPITUS USO SSGG.

C. López-Pernía acknowledges the financial support of MINECO through the FPI contract ref: BES-2016-078711. C. Muñoz-Ferreiro acknowledges the financial support of a VI PPIT-US fellowship through the contract USE-18740-H. Dr. F. Gotor and Dr. J.M. Córdoba are also gratefully acknowledged for providing access to the planetary ball mill.

REFERENCES

[1] C. Piconi, G. Maccauro, Zirconia as a ceramic biomaterial, Biomaterials. 20 (1999) 1–25. https://doi.org/10.1016/S0142-9612(98)00010-6.

[2] J. Chevalier, What future for zirconia as a biomaterial?, Biomaterials. 27 (2006) 535–543. https://doi.org/10.1016/j.biomaterials.2005.07.034.

[3] J. Chevalier, L. Gremillard, A. V. Virkar, D.R. Clarke, The tetragonal-monoclinic transformation in zirconia: Lessons learned and future trends, J. Am. Ceram. Soc. 92 (2009) 1901–1920. https://doi.org/10.1111/j.1551-

2916.2009.03278.x.

[4] S. Lawson, Environmental degradation of zirconia ceramics, J. Eur. Ceram. Soc. 15 (1995) 485–502. https://doi.org/10.1016/0955-2219(95)00035-S.

[5] X. Guo, Property degradation of tetragonal zirconia induced by low-temperature defect reaction with water molecules, Chem. Mater. 16 (2004) 3988–3994. https://doi.org/10.1021/cm040167h.

[6] N. Garmendia, S. Grandjean, J. Chevalier, L.A. Diaz, R. Torrecillas, I. Obieta, Zirconia-multiwall carbon nanotubes dense nano-composites with an unusual balance between crack and ageing resistance, J. Eur. Ceram. Soc. 31 (2011) 1009–1014. https://doi.org/10.1016/j.jeurceramsoc.2010.12.029.

[7] Z. Xia, L. Riester, W.A. Curtin, H. Li, B.W. Sheldon, J. Liang, B. Chang, J.M. Xu, Direct observation of toughening mechanisms in carbon nanotube ceramic matrix composites, Acta Mater. 52 (2004) 931–944. https://doi.org/10.1016/j.actamat.2003.10.050.

[8] C. Ramirez, P. Miranzo, M. Belmonte, M.I. Osendi, P. Poza, S.M. Vega-Diaz, M. Terrones, Extraordinary toughening enhancement and flexural strength in Si_3N_4 composites using graphene sheets, J. Eur. Ceram. Soc. 34 (2014) 161–169. https://doi.org/10.1016/j.jeurceramsoc.2013.08.039.

[9] A. Nieto, A. Bisht, D. Lahiri, C. Zhang, A. Agarwal, Graphene reinforced metal and ceramic matrix composites: a review, Int. Mater. Rev. 62 (2017) 241–302. https://doi.org/10.1080/09506608.2016.1219481.

[10] P. Miranzo, M. Belmonte, M.I. Osendi, From bulk to cellular structures: A review on ceramic/graphene filler composites, J. Eur. Ceram. Soc. 37 (2017) 3649–3672. https://doi.org/10.1016/j.jeurceramsoc.2017.03.016.

[11] Y. Liu, X. Jiang, J. Shi, Y. Luo, Y. Tang, Q. Wu, Z. Luo, Research on the interface properties and strengthening-toughening mechanism of nanocarbon-toughened ceramic matrix composites, Nanotechnol. Rev. 9 (2020) 190–208. https://doi.org/10.1515/ntrev-2020-0017.

[12] A.G. Glukharev, V.G. Konakov, O.Y. Kurapova, Electrical and mechanical properties of zirconia-graphene composites, Rev. Adv. Mater. Technol. 2 (2020) 27–41. https://doi.org/10.17586/2687-0568-2020-2-4-27-41.

[13] J.H. Shin, S.H. Hong, Fabrication and properties of reduced graphene oxide reinforced yttria-stabilized zirconia composite ceramics, J. Eur. Ceram. Soc. 34 (2014) 1297–1302. https://doi.org/10.1016/j.jeurceramsoc.2013.11.034.

[14] S. Li, Z. Xie, Y. Zhang, Y. Zhou, Enhanced toughness of zirconia ceramics with graphene platelets consolidated by spark plasma sintering, Int. J. Appl. Ceram. Technol. 14 (2017) 1062–1068. https://doi.org/10.1111/ijac.12742.

[15] F. Chen, D. Jin, K. Tyeb, B. Wang, Y.H. Han, S. Kim, J.M. Schoenung, Q. Shen, L. Zhang, Field assisted sintering of graphene reinforced zirconia ceramics, Ceram. Int. 41 (2015) 6113–6116. https://doi.org/10.1016/j.ceramint.2014.12.147.

[16] J. Su, Y. Chen, Q. Huang, Graphene nanosheet-induced toughening of yttria-stabilized zirconia, Appl. Phys. A. 123 (2017) 10.

https://doi.org/10.1007/s00339-016-0613-7.

[17] A. Leonov, M. Kalashnikov, J. Li, E. Abdulmenova, M. Rudmin, Y. Ivanov, Effect of carbon nanotubes and graphene nanoplatelets on the mechanical properties of zirconia-based composites, in: 2020 7th Int. Congr. Energy Fluxes Radiat. Eff., IEEE, 2020: pp. 1169–1173. https://doi.org/10.1109/EFRE47760.2020.9242000.

[18] Z. Zeng, Y. Liu, W. Chen, X. Li, Q. Zheng, K. Li, R. Guo, Fabrication and properties of in situ reduced graphene oxide-toughened zirconia composite ceramics, J. Am. Ceram. Soc. 101 (2018) 3498–3507. https://doi.org/10.1111/jace.15483.

[19] K. Jiang, J. Li, J. Liu, Spark plasma sintering and characterization of graphene platelet/ceramic composites, Adv. Eng. Mater. 17 (2015) 716–722. https://doi.org/10.1002/adem.201400326.

[20] S.M. Kwon, S.J. Lee, I.J. Shon, Enhanced properties of nanostructured ZrO_2-graphene composites rapidly sintered via high-frequency induction heating, Ceram. Int. 41 (2015) 835–842. https://doi.org/10.1016/j.ceramint.2014.08.042.

[21] N. Obradović, F. Kern, Properties of 3Y-TZP zirconia ceramics with graphene addition obtained by spark plasma sintering, Ceram. Int. 44 (2018) 16931–16936. https://doi.org/10.1016/j.ceramint.2018.06.133.

[22] J.S. Bunch, S.S. Verbridge, J.S. Alden, A.M. van der Zande, J.M. Parpia, H.G. Craighead, P.L. McEuen, Impermeable atomic membranes from graphene sheets, Nano Lett. 8 (2008) 2458–2462. https://doi.org/10.1021/nl801457b.

[23] Y. Su, V.G. Kravets, S.L. Wong, J. Waters, A.K. Geim, R.R. Nair, Impermeable barrier films and protective coatings based on reduced graphene oxide, Nat. Commun. 5 (2014) 4843. https://doi.org/10.1038/ncomms5843.

[24] V. Berry, Impermeability of graphene and its applications, Carbon N. Y. 62 (2013) 1–10. https://doi.org/10.1016/j.carbon.2013.05.052.

[25] C. Muñoz-Ferreiro, A. Morales-Rodríguez, T.C.T.C. Rojas, E. Jiménez-Piqué, C. López-Pernía, R. Poyato, A. Gallardo-López, Microstructure, interfaces and properties of 3YTZP ceramic composites with 10 and 20 vol% different graphene-based nanostructures as fillers, J. Alloys Compd. 777 (2019) 213–224. https://doi.org/10.1016/j.jallcom.2018.10.336.

[26] E. Mohamed, M. Taheri, M. Mehrjoo, M. Mazaheri, A.M. Zahedi, M.A. Shokrgozar, F. Golestani-Fard, In vitro biocompatibility and ageing of 3Y-TZP/CNTs composites, Ceram. Int. 41 (2015) 12773–12781. https://doi.org/10.1016/j.ceramint.2015.06.112.

[27] A. Morales-Rodríguez, R. Poyato, F. Gutiérrez-Mora, A. Muñoz, A. Gallardo-López, The role of carbon nanotubes on the stability of tetragonal zirconia polycrystals, Ceram. Int. 44 (2018) 17716–17723. https://doi.org/10.1016/j.ceramint.2018.06.238.

[28] S. Peretz Damari, L. Cullari, D. Laredo, R. Nadiv, E. Ruse, R. Sripada, O. Regev, Graphene and boron nitride nanoplatelets for improving vapor barrier properties in epoxy nanocomposites, Prog. Org. Coatings. 136 (2019) 105207.

https://doi.org/10.1016/j.porgcoat.2019.06.053.

[29] S. Prolongo, A. Jiménez-Suárez, R. Moriche, A. Ureña, Influence of thickness and lateral size of graphene nanoplatelets on water uptake in epoxy/graphene nanocomposites, Appl. Sci. 8 (2018) 1550. https://doi.org/10.3390/app8091550.

[30] N.T. Kirkland, T. Schiller, N. Medhekar, N. Birbilis, Exploring graphene as a corrosion protection barrier, Corros. Sci. 56 (2012) 1–4. https://doi.org/10.1016/j.corsci.2011.12.003.

[31] K.S. Aneja, H.L.M. Böhm, A.S. Khanna, S. Böhm, Functionalised graphene as a barrier against corrosion, FlatChem. 1 (2017) 11–19. https://doi.org/10.1016/j.flatc.2016.08.003.

[32] O.C. Compton, S. Kim, C. Pierre, J.M. Torkelson, S.T. Nguyen, Crumpled graphene nanosheets as highly effective barrier property enhancers, Adv. Mater. 22 (2010) 4759–4763. https://doi.org/10.1002/adma.201000960.

[33] B. Wang, B. V. Cunning, S.-Y. Park, M. Huang, J.-Y. Kim, R.S. Ruoff, Graphene coatings as barrier layers to prevent the water-induced corrosion of silicate glass, ACS Nano. 10 (2016) 9794–9800. https://doi.org/10.1021/acsnano.6b04363.

[34] B. Martín-García, Y. Bi, M. Prato, D. Spirito, R. Krahne, G. Konstantatos, I. Moreels, Reduction of moisture sensitivity of PbS quantum dot solar cells by incorporation of reduced graphene oxide, Sol. Energy Mater. Sol. Cells. 183 (2018) 1–7. https://doi.org/10.1016/j.solmat.2018.04.005.

[35] Q. Luo, Y. Zhang, C. Liu, J. Li, N. Wang, H. Lin, Iodide-reduced graphene oxide with dopant-free spiro-OMeTAD for ambient stable and high-efficiency perovskite solar cells, J. Mater. Chem. A. 3 (2015) 15996–16004. https://doi.org/10.1039/C5TA02710A.

[36] G. Kakavelakis, T. Maksudov, D. Konios, I. Paradisanos, G. Kioseoglou, E. Stratakis, E. Kymakis, Efficient and highly air stable planar inverted perovskite solar cells with reduced graphene oxide doped PCBM electron transporting layer, Adv. Energy Mater. 7 (2017) 1602120. https://doi.org/10.1002/aenm.201602120.

[37] A. Gallardo-López, I. Márquez-Abril, A. Morales-Rodríguez, A. Muñoz, R. Poyato, Dense graphene nanoplatelet/yttria tetragonal zirconia composites: Processing, hardness and electrical conductivity, Ceram. Int. 43 (2017) 11743–11752. https://doi.org/10.1016/j.ceramint.2017.06.007.

[38] Á. Gallardo-López, J. Castillo-Seoane, C. Muñoz-Ferreiro, C. López-Pernía, A. Morales-Rodríguez, R. Poyato, Flexure strength and fracture propagation in zirconia ceramic composites with exfoliated graphene nanoplatelets, Ceramics. 3 (2020) 78–91. https://doi.org/10.3390/ceramics3010009.

[39] C. López-Pernía, C. Muñoz-Ferreiro, C. González-Orellana, A. Morales-Rodríguez, Á. Gallardo-López, R. Poyato, Optimizing the homogenization technique for graphene nanoplatelet/yttria tetragonal zirconia composites: Influence on the microstructure and the electrical conductivity, J. Alloys Compd. 767 (2018) 994–1002. https://doi.org/10.1016/j.jallcom.2018.07.199.

[40] C. López-Pernía, A. Morales-Rodríguez, Á. Gallardo-López, R. Poyato,

Enhancing the electrical conductivity of in-situ reduced graphene oxide-zirconia composites through the control of the processing routine, Ceram. Int. 47 (2021) 9382–9391. https://doi.org/10.1016/j.ceramint.2020.12.069.

[41] S. Claramunt, A. Varea, D. López-Díaz, M.M. Velázquez, A. Cornet, A. Cirera, The importance of interbands on the interpretation of the Raman spectrum of graphene oxide, J. Phys. Chem. C. 119 (2015) 10123–10129. https://doi.org/10.1021/acs.jpcc.5b01590.

[42] C. Muñoz-Ferreiro, C. López-Pernía, Á. Gallardo-López, R. Poyato, Unravelling the optimization of few-layer graphene crystallinity and electrical conductivity in ceramic composites by Raman spectroscopy, J. Eur. Ceram. Soc. 41 (2021) 290–298.

[43] R.A. Young, The Rietveld method, International Union of Crystallography/Oxford University Press, New York, NY, USA, 1993.

[44] A. Bruker, TOPAS 5 user manual, Bruker AXS GmbH, Germany Search PubMed, Karlsruhe, 2014.

[45] H. Toraya, M. Yoshimura, S. Somiya, Calibration curve for quantitative analysis of the monoclinic-tetragonal ZrO_2 system by X-Ray diffraction, J. Am. Ceram. Soc. 67 (1984) C-119-C–121. https://doi.org/10.1111/j.1151-2916.1984.tb19715.x.

[46] R.C. Garvie, P.S. Nicholson, Phase analysis in zirconia systems, J. Am. Ceram. Soc. 55 (1972) 303–305. https://doi.org/10.1111/j.1151-2916.1972.tb11290.x.

[47] W.A. Johnson, R.F. Mehl, Reaction kinetics in processes of nucleation and growth, Trans. Am. Inst. Minning Metall. Eng. 135 (1939) 416–458.

[48] L. Gremillard, J. Chevalier, T. Epicier, S. Deville, G. Fantozzi, Modeling the aging kinetics of zirconia ceramics, J. Eur. Ceram. Soc. 24 (2004) 3483–3489. https://doi.org/10.1016/j.jeurceramsoc.2003.11.025.

[49] C. Muñoz-Ferreiro, A. Morales-Rodríguez, T.C. Rojas, E. Jiménez-Piqué, C. López-Pernía, R. Poyato, A. Gallardo-López, Microstructure, interfaces and properties of 3YTZP ceramic composites with 10 and 20 vol% different graphene-based nanostructures as fillers, J. Alloys Compd. 777 (2019) 213–224. https://doi.org/10.1016/j.jallcom.2018.10.336.

[50] R. Chintapalli, F.G. Marro, J.A. Valle, H. Yan, M.J. Reece, M. Anglada, Degradation resistance of 3Y-TZP ceramics sintered using spark plasma sintering, in: IOP Conf. Ser. Mater. Sci. Eng., 2009: p. 012014. https://doi.org/10.1088/1757-899X/5/1/012014.

[51] C. Casiraghi, A. Hartschuh, H. Qian, S. Pliscanec, C. Georgia, A. Fasoli, K.S. Novoselov, D.M. Basko, A.C. Ferrari, Raman spectroscopy of graphene edges, Nano Lett. 9 (2009) 1433–1441. https://doi.org/10.1021/nl8032697.

[52] B. Román-Manso, E. Domingues, F.M. Figueiredo, M. Belmonte, P. Miranzo, Enhanced electrical conductivity of silicon carbide ceramics by addition of graphene nanoplatelets, J. Eur. Ceram. Soc. 35 (2015) 2723–2731. https://doi.org/10.1016/j.jeurceramsoc.2015.03.044.

[53] R. Poyato, R. Verdugo, C. Muñoz-Ferreiro, Á. Gallardo-López,

Electrochemically exfoliated graphene-like nanosheets for use in ceramic nanocomposites, Materials (Basel). 13 (2020) 2656. https://doi.org/10.3390/ma13112656.

[54] X. Wang, J. Zhao, E. Cui, H. Liu, Y. Dong, Z. Sun, Effects of sintering parameters on microstructure, graphene structure stability and mechanical properties of graphene reinforced Al_2O_3-based composite ceramic tool material, Ceram. Int. 45 (2019) 23384–23392. https://doi.org/10.1016/j.ceramint.2019.08.040.

[55] E.H. Martins Ferreira, M.V.O. Moutinho, F. Stavale, M.M. Lucchese, R.B. Capaz, C.A. Achete, A. Jorio, Evolution of the Raman spectra from single-, few-, and many-layer graphene with increasing disorder, Phys. Rev. B. 82 (2010) 125429. https://doi.org/10.1103/PhysRevB.82.125429.

[56] A.C. Ferrari, J.C. Meyer, V. Scardaci, C. Casiraghi, M. Lazzeri, F. Mauri, S. Piscanec, D. Jiang, K.S. Novoselov, S. Roth, A.K. Geim, Raman spectrum of graphene and graphene layers, Phys. Rev. Lett. 97 (2006) 187401. https://doi.org/10.1103/PhysRevLett.97.187401.

[57] L.M. Malard, M.A. Pimenta, G. Dresselhaus, M.S. Dresselhaus, Raman spectroscopy in graphene, Phys. Rep. 473 (2009) 51–87. https://doi.org/10.1016/j.physrep.2009.02.003.

[58] Á. Gallardo-López, C. Muñoz-Ferreiro, C. López-Pernía, E. Jiménez-Piqué, F. Gutiérrez-Mora, A. Morales-Rodríguez, R. Poyato, Critical influence of the processing route on the mechanical properties of zirconia composites with graphene nanoplatelets, Materials (Basel). 14 (2021) 1–11. https://doi.org/10.3390/ma14010108.

[59] R. Poyato, J. Macías-Delgado, A. García-Valenzuela, R.L. González-Romero, A. Muñoz, A. Domínguez-Rodríguez, Electrical properties of reduced 3YTZP ceramics consolidated by spark plasma sintering, Ceram. Int. 42 (2016) 6713–6719. https://doi.org/10.1016/j.ceramint.2016.01.040.

[60] J.F. Bartolomé, I. Montera, M. Díaz, S. López-Esteban, J.S. Moya, S. Deville, L. Gremillard, J. Chevalier, G. Fantozzi, Accelerated aging in 3-mol%-yttria-stabilized tetragonal zirconia ceramics sintered in reducing conditions, J. Am. Ceram. Soc. 87 (2004) 2282–2285. https://doi.org/10.1111/j.1151-2916.2004.tb07505.x.

[61] S. Ubenthiran, M. Thanihaichelvan, R. Singh, Effect of air and argon sintering atmospheres on properties and hydrothermal aging resistance of Y-TZP ceramics, J. Mater. Eng. Perform. 27 (2018) 3574–3580. https://doi.org/10.1007/s11665-018-3428-1.

[62] J. Chevalier, Critical effect of cubic phase on aging in 3mol% yttria-stabilized zirconia ceramics for hip replacement prosthesis, Biomaterials. 25 (2004) 5539–5545. https://doi.org/10.1016/j.biomaterials.2004.01.002.

[63] C. Wei, L. Gremillard, Towards the prediction of hydrothermal ageing of 3Y-TZP bioceramics from processing parameters, Acta Mater. 144 (2018) 245–256. https://doi.org/10.1016/j.actamat.2017.10.061.

[64] B. Basu, Toughening of yttria-stabilised tetragonal zirconia ceramics, Int. Mater.

Rev. 50 (2005) 239–256. https://doi.org/10.1179/174328005X41113.

[65] S. Rani, M. Kumar, S. Sharma, D. Kumar, Role of graphene in structural transformation of zirconium oxide, J. Sol-Gel Sci. Technol. 71 (2014) 470–476. https://doi.org/10.1007/s10971-014-3401-x.

[66] D.N. Wang, K.M. Liang, The effect of carbon on the phase stability of zirconia, J. Mater. Sci. Lett. 17 (1998) 343–344. https://doi.org/10.1023/A:1006506411285.

[67] F. Inam, T. Vo, B.R. Bhat, Structural stability studies of graphene in sintered ceramic nanocomposites, Ceram. Int. 40 (2014) 16227–16233. https://doi.org/10.1016/j.ceramint.2014.07.058.

[68] C. Androulidakis, E.N. Koukaras, J. Parthenios, G. Kalosakas, K. Papagelis, C. Galiotis, Graphene flakes under controlled biaxial deformation, Sci. Rep. 5 (2016) 18219. https://doi.org/10.1038/srep18219.

[69] V. Lughi, V. Sergo, Low temperature degradation -aging- of zirconia: A critical review of the relevant aspects in dentistry, Dent. Mater. 26 (2010) 807–820. https://doi.org/10.1016/j.dental.2010.04.006.

[70] S. Ramesh, K.Y. Sara Lee, C.Y. Tan, A review on the hydrothermal ageing behaviour of Y-TZP ceramics, Ceram. Int. 44 (2018) 20620–20634. https://doi.org/10.1016/j.ceramint.2018.08.216.

[71] J. Eichler, J. Rödel, U. Eisele, M. Hoffman, Effect of grain size on mechanical properties of submicrometer 3Y-TZP: Fracture strength and hydrothermal degradation, J. Am. Ceram. Soc. 90 (2007) 2830–2836. https://doi.org/10.1111/j.1551-2916.2007.01643.x.

[72] ISO 13356:2008. Implants for surgery—Ceramic materials based on yttria-stabilized tetragonal zirconia (Y-TZP), (n.d.). https://scholar.google.com/scholar?q=ISO 13356:2008. Implants for surgeryCeramic materials based on yttria-stabilized tetragonal zirconia .

[73] S. Ramesh, M.M. Khan, H.C. Alexander Chee, Y.H. Wong, P. Ganesan, M.G. Kutty, U. Sutharsini, W.J.K. Chew, A. Niakan, Sintering behaviour and properties of graphene oxide-doped Y-TZP ceramics, Ceram. Int. 42 (2016) 17620–17625. https://doi.org/10.1016/j.ceramint.2016.08.077.